nanomaterials

MDPI

Article

Ultrafast Antisolvent Growth of Single-Crystal $CsPbBr_3$ Microcavity for Whispering-Gallery-Mode Lasing

Li Zhang [1], Xinxin Li [2], Yimeng Song [3] and Bingsuo Zou [4,*]

[1] School of Materials Science and Engineering, Beijing Institute of Technology, Beijing 100081, China; 3120195600@bit.edu.cn
[2] Key Laboratory for Renewable Energy, Beijing Key Laboratory for New Energy Materials and Devices, Beijing National Laboratory for Condensed Matter Physics, Institute of Physics, Chinese Academy of Sciences, Beijing 100190, China; xinxin.li@iphy.ac.cn
[3] Guangdong Provincial Key Laboratory of Electronic Functional Materials and Devices, Huizhou University, Huizhou 516001, China; b20180340@xs.ustb.edu.cn
[4] State Key Laboratory of Featured Metal Materials and Life-Cycle Safety for Composite Structures, Guangxi Key Laboratory of Processing for Nonferrous Metals and Featured Materials, School of Resources, Environments and Materials, Guangxi University, Nanning 530004, China
* Correspondence: zoubs@gxu.edu.cn

Abstract: In recent years, all-inorganic cesium lead bromide ($CsPbBr_3$) perovskites have garnered considerable attention for their prospective applications in green photonics and optoelectronic devices. However, the development of efficient and economical methods to obtain high-quality micron-sized single-crystalline $CsPbBr_3$ microplatelets (MPs) has become a challenge. Here, we report the synthesis of $CsPbBr_3$ MPs on Si/SiO_2 substrate by optimizing the ultrafast antisolvent method (FAS). This technique is able to produce well-dispersed, uniformly sized, and morphologically regular tetragonal phase single crystals, which can give strong green emission at room temperature, with excellent stability and excitonic character. Moreover, the crystals demonstrated lasing with a whispering gallery mode with a low threshold. These results suggest that the single-crystalline $CsPbBr_3$ MPs synthesized by this method are of high optical quality, holding vast potential for future applications in photonic devices.

Keywords: perovskites; fast growth; microstructures; lasing; photonics

Citation: Zhang, L.; Li, X.; Song, Y.; Zou, B. Ultrafast Antisolvent Growth of Single-Crystal $CsPbBr_3$ Microcavity for Whispering-Gallery-Mode Lasing. *Nanomaterials* **2023**, *13*, 2116. https://doi.org/10.3390/nano13142116

Received: 17 June 2023
Revised: 11 July 2023
Accepted: 19 July 2023
Published: 20 July 2023

1. Introduction

Small lasers show great application potential in optical integration, high-speed communication, and high-resolution imaging. Over the past few decades, a wide variety of semiconductor nanostructures, including nanowires, nanoribbons, and quantum dots, have been used as active materials for small lasers [1–6]. Recently, lead halide perovskites have attracted considerable interest in photovoltaics research due to their high absorption coefficient, substantial carrier diffusion length, and minimal density of defects. These properties make them highly suitable for efficient light absorption and carrier transport, which are crucial for photovoltaic applications. Additionally, perovskites exhibit superior gain performance, making them excellent candidates for coherent light sources [7–9]. Their superior gain performance also positions them as key contenders for efficient coherent light sources. Perovskite-based miniaturized lasers have been successfully developed utilizing various micro/nanostructures like nanowires, nanoplatelets, and quantum dots, all operating efficiently at room temperature [10–13]. When compared with traditional II-VI/III-V semiconductors, these optically pumped perovskite micro-lasers have demonstrated impressive advantages such as a lower lasing threshold, improved spectral coherence, and a broad spectrum of emission colours.

In recent years, all-inorganic perovskites, particularly $CsPbX_3$ (where X = Cl, Br, and I), have emerged as promising materials for various optoelectronic applications. One of the

main reasons for their growing preference over hybrid organic–inorganic perovskites is their superior electronic properties and enhanced stability against environmental factors such as moisture, oxygen, and heat [14–16]. As a result, these materials are particularly favoured for laser gain materials, which hold promising applications in areas like on-chip optical communication, sensors, and computing [17–19]. Over the past few years, there have been significant advancements in the field, with amplified spontaneous emission and lasing action being reported in $CsPbX_3$ thin films [20,21]. More recently, lasing action has been observed in $CsPbX_3$ micro/nanostructures, including micro/nanowires, nanorods, nanoplatelets, and microspheres [22,23]. To date, both Fabry-Pérot (F-P) and whispering-gallery-mode (WGM) lasers have been achieved in these $CsPbX_3$ microcavities [11,24]. Notably, WGM cavities offer advantages over F-P cavities due to their high-quality factor and compact size, which contribute to lasers with narrow linewidth and low thresholds.

At present, the main methods for synthesizing microcrystal $CsPbBr_3$ MPs are an antisolvent method, a space-confined growth strategy, and templated assembly [25–27]. Previously, we were successful in fabricating microcrystal $CsPbCl_3$ through an optimized ultrafast antisolvent method (FAS), and the mechanism is analysed deeply [28]. However, the application of this technique to other perovskites has been hindered due to their excessive solubility in DMF and the relatively constrained space during their crystallization process, which includes nucleation and growth phases. These issues result in significant interferences, causing the perovskite crystals to stack and ultimately deteriorating the quality of individual $CsPbBr_3$ MPs. Hence, it is of paramount importance to enhance the ultrafast antisolvent method to overcome these challenges.

Herein, to solve this issue, we added chlorobenzene (CB) to the precursor solution to reduce the solubility of perovskite and successfully prepared a highly dispersed $CsPbBr_3$ MP. The single crystal $CsPbBr_3$ MPs are evenly dispersed on the substrate, and the size ranges from 8 to 25 μm, presenting a regular geometric appearance. Strong photoluminescence (PL) spectroscopy is observed at 78–298 K, which is ascribed to the recombination of excitons. Moreover, the precisely defined geometry and smooth surface facilitate the operation of WGM lasing at room temperature. The $CsPbBr_3$ MP shows excellent stability under laser pulse and ambient air. These findings suggest that $CsPbBr_3$ MPs, synthesized using the FAS, hold substantial promise for applications in the realms of integrated photonics and optoelectronics.

2. Materials and Methods

2.1. Materials

CsBr and $PbBr_2$ were purchased from Aladdin (Shanghai, China). Dimethyl formamide (DMF), dichloromethane, chlorobenzene, ethanol, and acetone were purchased from Macklin (Shanghai, China).

2.2. Instrumentation

The surface structure of the synthesized samples was examined using a scanning electron microscope (SEM) via the Hitachi Instruments SU5000 (Japan), operating at a voltage of 20 kV. This was paired with energy-dispersive spectrometer (EDS) mapping to visualize the spatial distribution of various elements. Additionally, an atomic force microscope (AFM) from Bruker (Multimode8, Germany) was used to analyse surface roughness and particle thickness, operating in a scan analysis mode. The crystalline structure of the microparticles (MPs) was determined by acquiring X-ray diffraction (XRD) spectra, utilizing a PANalytical Empyrean XRD instrument (Netherlands). Transmission electron microscopy (TEM) analyses were carried out at 200 KV using a JEOL-2010F field-emission type high-resolution TEM (Japan).

X-ray photoelectron spectroscopy (XPS) was used to measure core level and VB spectra with the assistance of a Thermo Fisher Scientific ESCALAB 250X (Thermo Fisher Scientific, Waltham, MA, USA) equipped with a spherical quartz monochromator and energy analyse

working in the range of binding energies from 0 to 1500 eV. The energy resolution was $\Delta E \leq 0.5$ eV. The samples were measured at a pressure of 10^{-7} Pa.

The photoluminescence (PL) and lasing spectra were evaluated using a custom-built confocal micro-spectrometer setup. A solid-state laser with a continuous wavelength of 405 nm was employed for the steady-state PL tests, with the laser spot being concentrated onto the samples via a 100× Olympus objective lens (numerical aperture: 0.95, Japan). The PL spectra were gathered using the same lens in a backscattering configuration, then analysed through a monochromator fitted with a charge-coupled device detector (Japan) cooled by liquid nitrogen. For experiments conducted at lower temperatures, the samples were affixed within a liquid-flow micro-cryostat (CFM-1738-102, CRYO Industries, Manchester, NH, USA). Conducting lasing measurements, a 400 nm femtosecond pulsed laser, generated by the Coherent Astrella regenerative amplifier (800 nm, 100 fs, 1 kHz, USA), served as the excitation source. The laser spot was honed onto the samples with the aid of a 50× Olympus objective lens (numerical aperture: 0.45), producing a spot with a diameter of approximately 30 µm.

2.3. Synthesis Method

Figure 1 shows the schematic diagram of $CsPbBr_3$ MPs synthesis by FAS. Initially, 1 mmol each of CsBr and $PbBr_2$ were measured. These were mixed into 1 mL of DMF, and the solution was stirred at a temperature of 80 °C for 12 h. Then, the precursor was filtered, resulting in a clear solution. To this solution, 20 µL CB was added in order to adjust the solution to its saturation. After allowing the solution to settle, the resulting clear filtrate was then utilized as the precursor for $CsPbBr_3$. The Si/SiO_2 substrate (1.5 cm × 1.5 cm) was meticulously cleaned using a series of solvents, beginning with acetone, then alcohol, and finally, deionized water. Each cleaning process was performed for 15 min. After cleaning, the Si/SiO_2 substrate was dried using nitrogen gas, followed by a hydrophilic treatment using plasma to enhance surface properties. Then, the cleaned Si/SiO_2 substrate was then positioned on a heated stage set to maintain a steady temperature of 50 °C. After the temperature had stabilized, 20 µL saturated precursor was carefully added, swiftly followed by the addition of 10 µL CH_2Cl_2. Following the evaporation of solutions, a layer of $CsPbBr_3$ MPs was successfully formed on the surface of the Si/SiO_2 substrate.

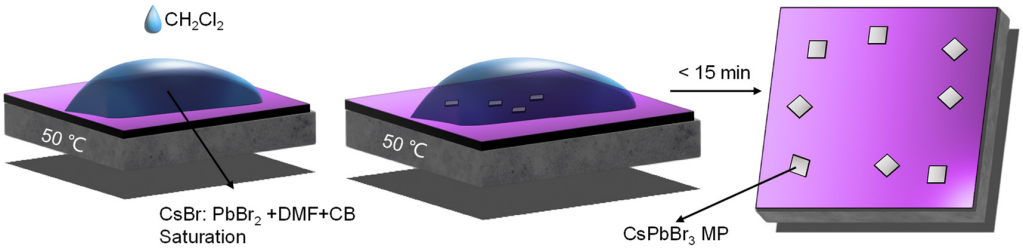

Figure 1. Schematic diagram of the $CsPbBr_3$ MP.

3. Results and Discussion

3.1. Morphology and Structure Characteristics

Figure 2 shows the morphologic characteristics of $CsPbBr_3$ MPs synthesized by FSA. The large-area SEM image (Figure 2a) confirms that the samples exhibit uniform dispersion across the Si/SiO_2 substrate, with no evident signs of agglomeration, and the as-fabricated $CsPbBr_3$ MPs exhibit uniformly rectangular shapes. Furthermore, the distribution of sizes across the samples is consistently uniform. These observations underscore the reliability and precision of the rapid antisolvent method used for synthesis, ensuring consistent sample production. The individual $CsPbBr_3$ MP energy-dispersive spectroscopy (EDS) mappings demonstrate that the distributions of Cs, Pb, and Br are evenly spread throughout the entire MP, as illustrated in Figure 2b. The fabrication processes of $CsPbCl_3$ MP include

two steps: nucleation and nuclei growth. The nucleation rate can be expressed as the following formula [29]:

$$\frac{dN}{dt} = Aexp\left(\frac{-\Delta G}{k_b T}\right) = A\ exp\left(\frac{16\pi\gamma^3 V_m^2}{3k_b^3 T^3 N_A^2 (lnS)^2}\right),$$

where N is the number of nuclei, A is the pre-exponential factor, k_b is the Boltzmann constant, N_A is the Avogadro constant, S is the degree of supersaturation, and T is the temperature. According to this equation, the main factors affecting the number of nucleation are T and S. The additive of antisolvent increases S, leading to the formation of a large number of crystal nuclei, which grows into MP with the evaporation of precursor solution. The rate of precursor solution is controlled by T. When the CB is incorporated into the precursor, its concentration diminishes. As the antisolvent is introduced, the number of nuclei produced will be greatly reduced. This arrangement ensures that during the ensuing growth process, each nucleus has ample space and resources for growth, thereby guaranteeing both its crystal quality and size.

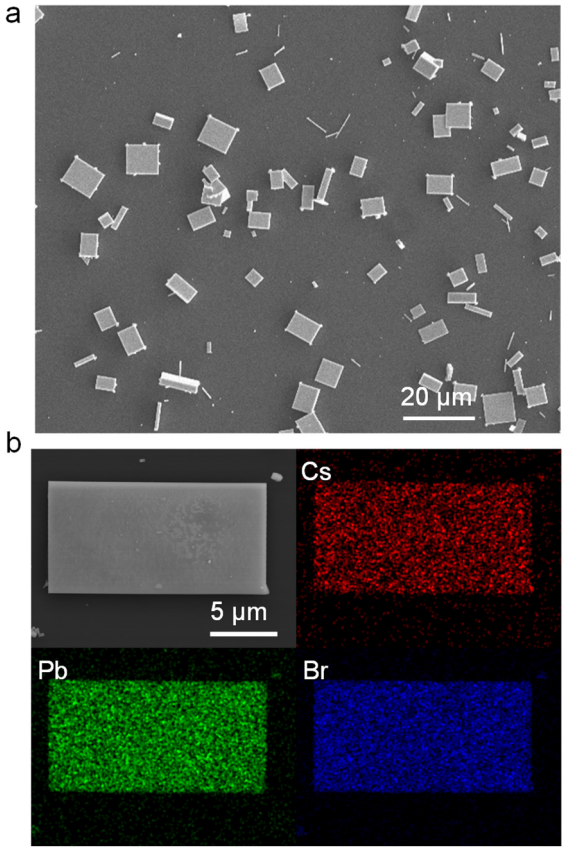

Figure 2. Morphology characterizations of FAS-fabricated $CsPbBr_3$MPs. (**a**) Large-area SEM image. (**b**) SEM image of single $CsPbBr_3$ MP and the corresponding elemental mapping of Cs, Pb, and Br, respectively.

CB was incorporated into our approach to regulating the concentration of the precursor, with two primary motivations behind this decision. First, CB is frequently employed as an antisolvent in perovskite synthesis, and its inclusion is known to facilitate certain enhancements in the surface quality of the perovskite. Second, given that CB possesses a slightly lower boiling point (132 °C) than DMF (153 °C), it prevents the re-dissolution of perovskite following initial evaporation, thereby preserving the final morphology of $CsPbBr_3$ MPs.

XPS is used to determine the structural composition of the heterojunction single crystals shown in Figure 3a. In Figure 3b–d, several distinct characteristic peaks exist in the representative XPS spectrum of the $CsPbBr_3$ MPs, which should come from the Cs 3d (3/2 and 5/2), Pb 4f (5/2 and 7/2), and Br 3d (3/2 and 5/2) core orbital levels of the $CsPbBr_3$ materials [30]. The binding energies for the Cs 3d, Pb 4f, and Br 3d regions are consistent with $CsPbBr_3$. In addition, the molar ratio of Cs, Pb, and Br atoms was calculated to be 1:1:3 based on this XPS spectrum, which is in good agreement with the stoichiometric $CsPbBr_3$.

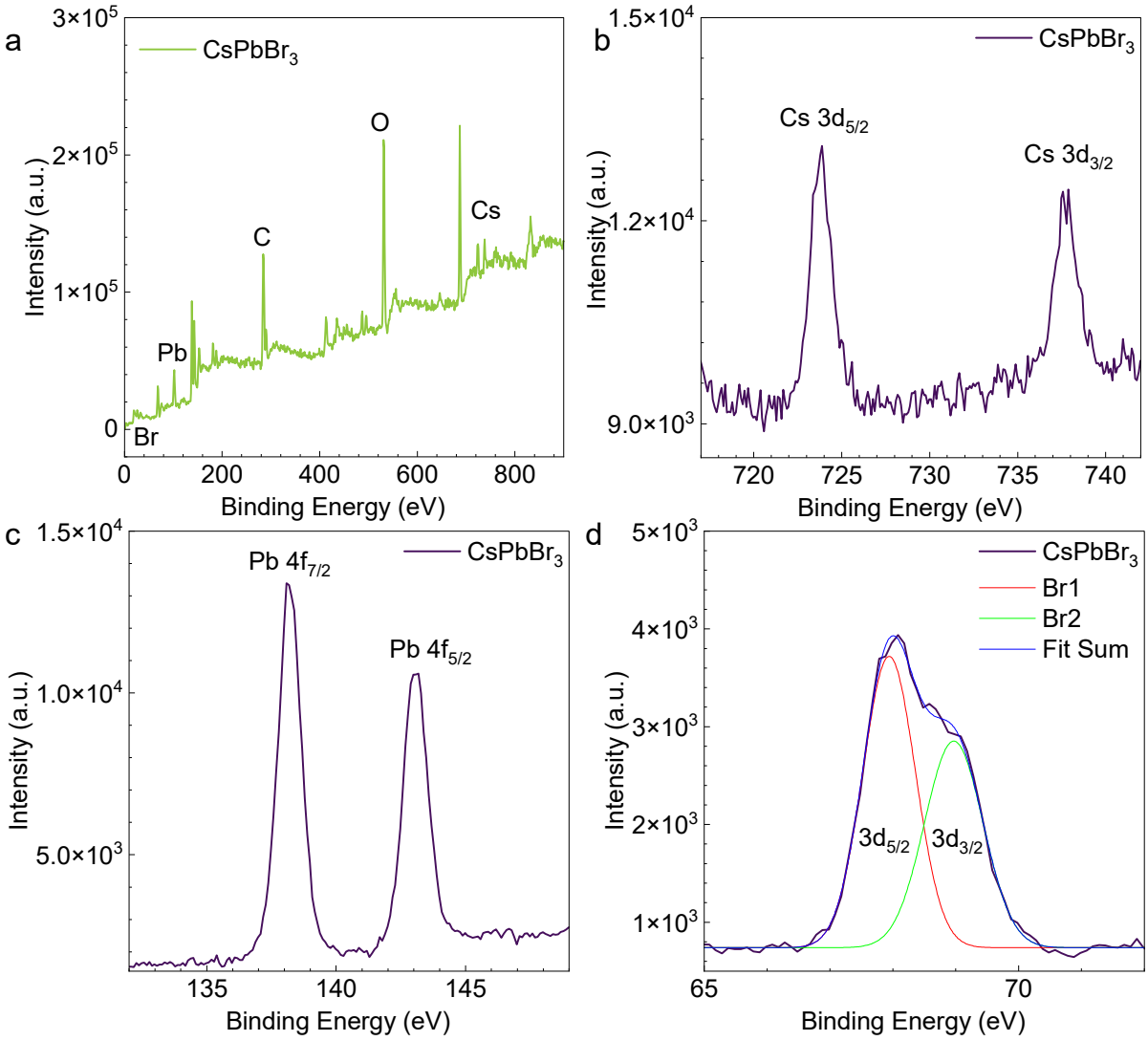

Figure 3. The XPS spectra of FAS-fabricated $CsPbBr_3$ MPs. (**a**) XPS characterization of the $CsPbBr_3$ MPs. (**b**–**d**) Corresponding XPS spectra of Cs 3d, Pb 4f, and Br 3d showing identical chemical bonding.

To investigate the crystal structure and growth mechanism of directional $CsPbBr_3$ MPs, we implemented X-ray diffraction (XRD) and transmission electron microscopy (TEM) characterizations. As shown in Figure 4a, all the $CsPbBr_3$ MPs' sharp diffraction peaks are indexed to the tetragonal perovskite phase of $CsPbBr_3$ [31]. Three peaks are resolved at 15.2°, 30.3°, and 30.7°, which index to (001), (002), and (200) planes of the orthorhombic phase of $CsPbBr_3$, respectively. Figure 4b shows the high-resolution TEM image and the measured lattice spacings of the $CsPbBr_3$ MP is approximately 0.58 nm, corresponding to (001) lattice planes of tetragonal perovskite $CsPbBr_3$.

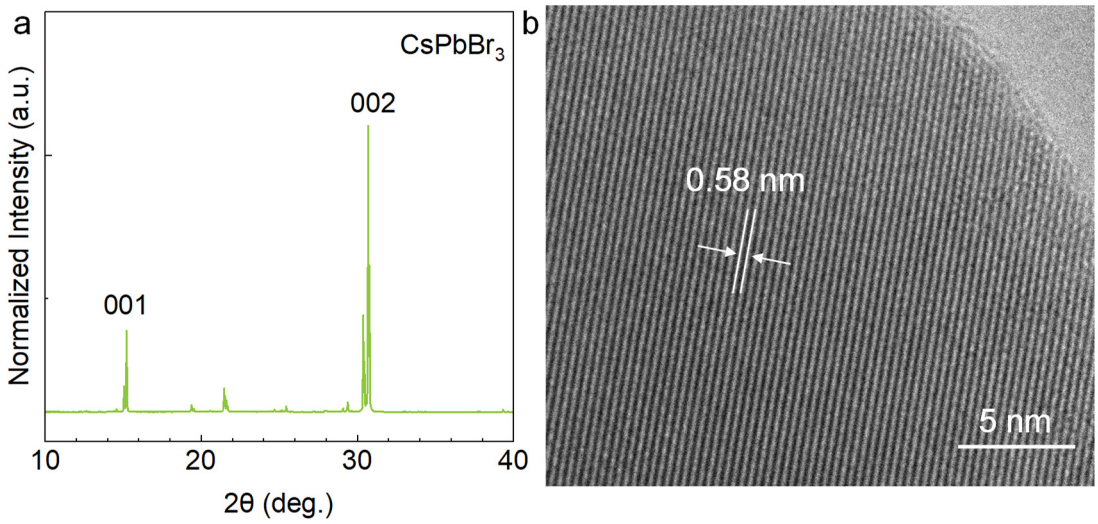

Figure 4. Structure characterizations of FAS-fabricated $CsPbBr_3$ MPs. (**a**) XRD pattern. (**b**) The high-resolution TEM image.

3.2. Optical Characteristics

Figure 5a shows the temperature-dependent PL of single $CsPbBr_3$ MP from 78 K to 298 K. The PL spectra were asymmetric in shape with a main peak at ~2.33 eV and a shoulder at ~2.37 eV under 298 K. Via Gaussian fitting, two peaks are obtained, which are Peak 1 (high energy) and Peak 2 (low energy), respectively. Based on the position of the peaks and the trend of increasing intensity with temperature, we assume that both peaks are from exciton emission [32]. The variation in peak energy with temperature from 78 K through 298 K for the two peaks is shown in Figure 5b. Thermal expansion and electron–phonon interaction lead to the change in the band gap of the semiconductor with temperature [33]. When the temperature is reduced from 298 K to 200 K, thermal expansion is a dominating factor. Thermal expansion of the lattice tends to increase the interaction between two valence orbitals (s and p), which leads to narrowing the valence bandwidth and, hence, the forbidden gap decreases [34]. In the meantime, as temperature decreases, electron–phonon scattering is lower, leading to the redshift of the emission peak [35]. The change of peak position is due to lattice thermal expansion and electron–phonon coupling. The free excitons are band recombination, and the conduction band and valence band are sensitive to the change in temperature. Figure 5b, both Peak 1 and Peak 2 broaden monotonically with the increasing temperature. The energy difference between Peak 1 and Peak 2 is about 10 meV at 78 K, and as the temperature increases, the energy difference becomes larger, and the energy difference is about 40 meV at 298 K. In addition, Peak 2 shows a significant redshift from 200 K to 298 K, indicating that the electron–phonon coupling is dominant as the temperature increases; that is, the electron–phonon coupling strength is higher than that of the free exciton. Therefore, Peak 2 is likely to be a localized exciton. [36,37]. The temperature-dependent PL study gives information about the physical parameters of $CsPbBr_3$ such as exciton binding energy (E_b), longitudinal optical phonon energy (E_{ph}), inhomogeneous broadening (Γ_0), and exciton–phonon coupling strength (Γ_{op}). As expected, PL intensity for all peaks decreases with increasing temperature. The PL intensity as a function of temperature is plotted and fitted using an Arrhenius equation [38]:

$$I(T) = \frac{I_0}{1 + Aexp[-E_b/k_bT]}$$

where I_0 is the PL intensity at 0 K, E_b is the activation energy, and k_b is the Boltzmann constant. Here, the exciton binding energy E_b of Peak 1 can be fitted as 45.9 meV. These values were very close to the binding energy (40 meV) previously reported for $CsPbBr_3$, indicating the significant contribution of thermal dissociation of excitons to the decrease

in PL intensities [39]. Assessing the temperature-dependent emission broadening in Figure 5d,e, the intrinsic FWHM (Γ_0) of both peaks grows with increasing temperatures. The Peak 1 emission broadens faster than Peak 2 with rising temperature, suggesting enhanced carrier scattering in these bands [40,41]. The temperature-dependent excitonic line width of band-to-band transitions within semiconductors is relatively well understood, being described by a Boson model [42]:

$$\Gamma(T) = \Gamma_0 + \sigma T + \Gamma_{op} / \left(exp\left(E_{op}/k_b T\right) - 1\right)$$

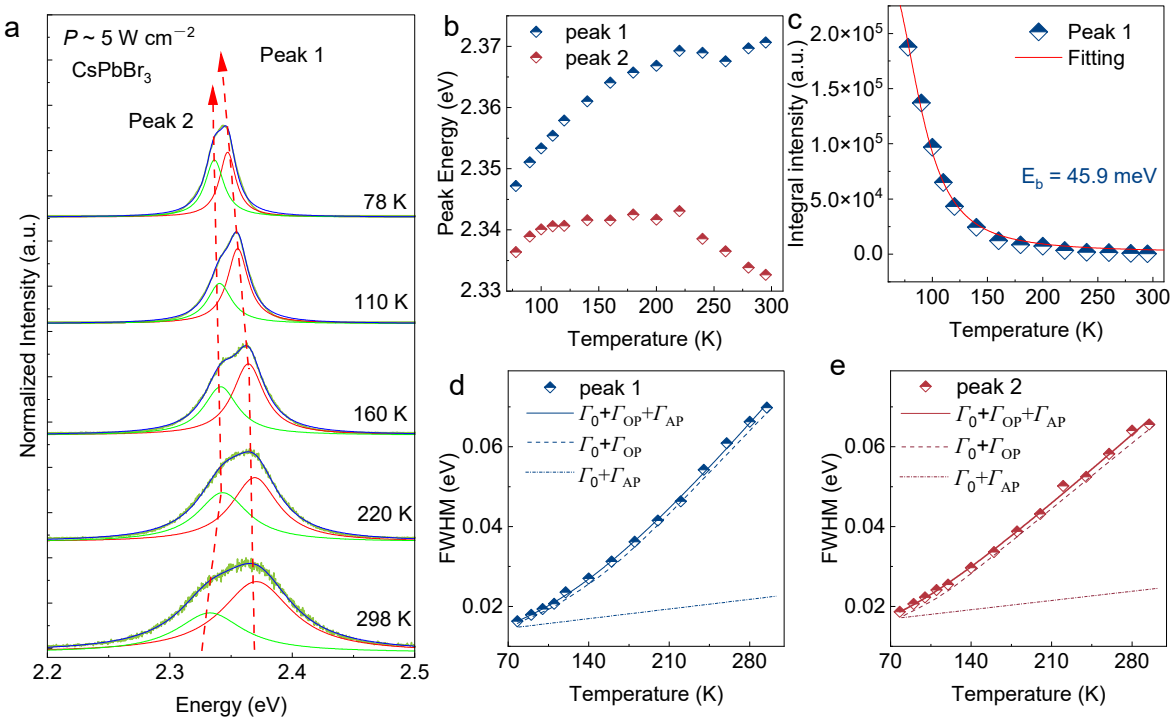

Figure 5. Temperature-dependent PL spectra of FAS-fabricated $CsPbBr_3$MP. (**a**) Temperature-dependent PL spectra of single $CsPbBr_3$ MP in the temperature range of 78–298 K (CW laser 405 nm). (**b**) Emission energy of two PL emission peaks. (**c**) Integral PL intensities of Peak 1 specimens recorded at low temperatures. FWHM of PL bands recorded from (**d**) Peak 1, and (**e**) Peak 2 specimens at low temperatures.

In this equation, the three terms from left to right denote the contributions of inhomogeneous broadening, acoustic phonons, and optical phonons, respectively, with σ the exciton–acoustic phonon interaction coefficient, Γ_{op} the exciton–optical phonon coupling coefficient, and E_{op} the average optical phonon energy. The fitted values of Γ_0, σ, Γ_{op}, and E_{op} are summarized in Table 1.

Table 1. The fitted parameters of Peak 1 and Peak 2.

	Γ_0 (meV)	σ (meV/T)	Γ_{op} (meV)	E_{op} (meV)
Peak 1	7.88	0.104	58.8	41.7
Peak 2	14.4	0.158	60.5	20.0

This shows that the linewidth of the two peaks mainly comes from the exciton–phonon interaction.

3.3. Lasing

To obtain the laser characteristics of the sample, we used a 400 nm, 1 kHz femtosecond laser as the pump source to excite an individual $CsPbBr_3$ MP, and all tests were performed at room temperature. The evolution of the PL spectral profile with the pump fluence is shown in Figure 6a. The PL spectrum is characterized by a broad spontaneous emission band centre at ~535 nm with the FWHM of ~20 nm when the $CsPbBr_3$ MP is pumped at low pump fluences. When the pump fluence is increased up to 39.5 μJ cm^{-2}, a new narrow peak begins to emerge at ~540 nm. When the pump fluence is further increased, the new-emerging narrow peak centre at ~540 nm becomes dominant over the spontaneous emission background. The peak is well-fitted by a Gauss function with an FWHM of 0.6 nm. The Q factor was calculated to be ≈ 913.3 using the equation $Q = \lambda/\Delta\lambda$, where λ is the peak centre wavelength and $\Delta\lambda$ is the peak width. Figure 6a inset that bright green emission from the rod ends was observed under an excitation density higher than P_{th}. In a square WGM resonator, the mode spacing $\Delta\lambda$ at wavelength λ is given by [43,44]:

$$\Delta\lambda = \frac{\lambda^2}{2\sqrt{2n_g L}}$$

where n_g is the group refractive index. The mode spacing $\Delta\lambda$ between two adjacent modes decreases with the increase in the edge length L. When the excitation fluence surpasses the lasing threshold, spontaneous emission is selected and restricted by the WGM cavity. This restriction causes a large amount of photons to only be released from the edges of the square cavity [45]. As a result, the micro-pillar edge, and especially the corners, exhibit significantly stronger emissions [11]. The $CsPbBr_3$ Mott density (1.8×10^{17} to 4.7×10^{17} cm^{-3}), results in the electron–hole plasma, which is also its gain characteristic. In our report, the lasing threshold was derived at ~34.1 μJ cm^{-2} and then the carrier density at the threshold of the $CsPbBr_3$ MP was estimated to be 6.2×10^{19} cm^{-3}. Therefore, this is the main cause of the redshift of the laser mode [46]. Figure 6b plots the PL intensity and FWHM as a function of the pumping density. An inflection point can be observed during the pumping density increase procedure, confirming the evolution from spontaneous emission to stimulated emission at ≈34.1 μJ cm^{-2}. At this point, the FWHM will also dramatically decrease. Figure 6c is a statistical diagram of the threshold of random $CsPbBr_3$ MP. The threshold of the sample varies from 30–60 μJ cm^{-2}, which is attributed to the difference in size of $CsPbBr_3$ MP [47,48].

3.4. Stability

Long-term working stability is significantly important for practical application. As shown in Figure 7a, the $CsPbBr_3$ MP shows excellent optical stability with the PL intensity sustained for more than 180 min, corresponding to 1.08×10^7 laser shots. The PL intensity measured at 0 and 180 min shows almost identical. Interestingly, the PL intensity of $CsPbBr_3$ MP tended to increase first with the excitation density, possibly due to humidity-induced self-healing of the perovskite lattice or the photocuring phenomenon [49,50]. The $CsPbBr_3$ MP without any encapsulation retained 95% of its original PL in ambient conditions for 12 weeks (Figure 7b). We believe the smaller specific surface area and the small number of defects in the $CsPbBr_3$ MP are the key points that make it more stable than other nanostructured perovskite materials. The above results demonstrate that the large $CsPbBr_3$ MPs have great potential for practical applications in nonlinear optical devices.

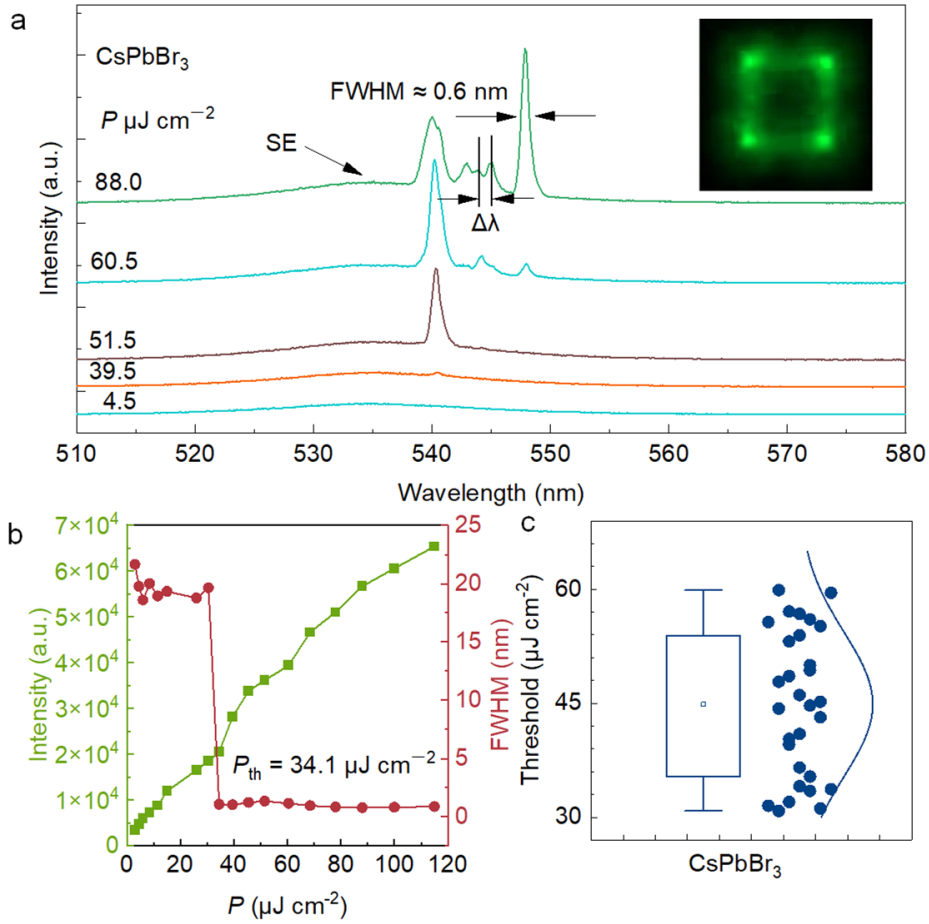

Figure 6. Lasing of single $CsPbBr_3$MPs. (**a**) PL spectra of a FAS-fabricated $CsPbBr_3$ MP at pump densities of 4.5, 39.5, 51.5, 60.5, and 88.0 μJ cm^{-2}, respectively. Inset: PL emission image above threshold. Length of MP side ≈ 10 μm. (**b**) Integrated PL intensity and FWHM as a function of pump density ranging from 3.0 to 115.0 μJ cm^{-2}. The threshold is ≈34.1 μJ cm^{-2}. (**c**) Threshold statistics of FAS-fabricated $CsPbBr_3$ MPs.

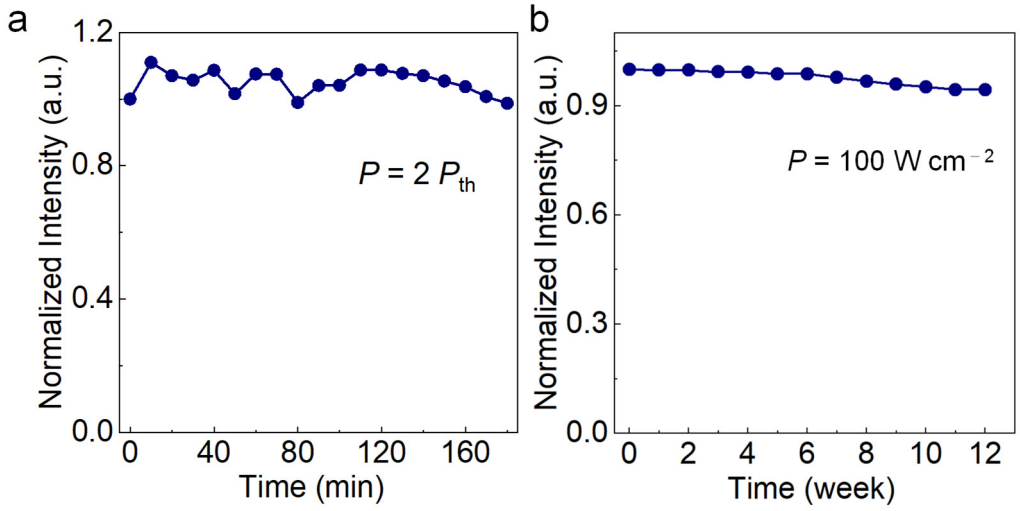

Figure 7. Stability of FAS-fabricated $CsPbBr_3$ MPs. (**a**) Normalized PL intensity of the $CsPbBr_3$ MP under pulsed laser excitation at 2 P_{th}. (**b**) Normalized PL stability of the $CsPbBr_3$ MP at room temperature under 405 nm CW lasing.

4. Conclusions

In this study, we successfully synthesized monodispersed $CsPbBr_3$ MPs on Si/SiO_2 substrate by optimizing the rapid antisolvent technique, paying particular attention to understanding the role of CB in the process. Temperature-dependent PL analysis elucidated that the exciton binding energy and linewidth are predominantly governed by exciton-photon interactions. Furthermore, we achieved a WGM laser with a threshold of 34.1 μJ cm^{-2} at room temperature. Remarkably, the PL intensity remained largely unaltered after 12 weeks of environmental exposure. These findings collectively suggest that $CsPbBr_3$ MPs prepared by this method possess significant potential for applications in integrated photonics and optoelectronic devices.

Author Contributions: L.Z.: design experiment, PL spectral and laser, stability test and writing—original draft. X.L.: XRD and SEM. Y.S.: TEM and XPS. B.Z.: funding acquisition and revising the manuscript. All authors have read and agreed to the published version of the manuscript.

Funding: We thanks the National Natural Science Foundation of China (Grant Nos. 62004218), the Strategic Priority Research Program of Chinese Academy of Sciences (Grant No. XDB33000000) and Youth Innovation Promotion Association CAS.

Data Availability Statement: All data are available in the manuscript.

Conflicts of Interest: The authors declare no conflict of interest.

References

1. Duan, X.F.; Huang, Y.; Agarwal, R.; Lieber, C.M. Single-nanowire electrically driven lasers. *Nature* **2003**, *421*, 241–245. [CrossRef] [PubMed]
2. Guzelturk, B.; Kelestemur, Y.; Gungor, K.; Yeltik, A.; Akgul, M.Z.; Wang, Y.; Chen, R.; Dang, C.; Sun, H.D.; Demir, H.V. Stable and Low-Threshold Optical Gain in CdSe/CdS Quantum Dots: An All-Colloidal Frequency Up-Converted Laser. *Adv. Mater.* **2015**, *27*, 2741–2746. [CrossRef] [PubMed]
3. Huang, M.H.; Mao, S.; Feick, H.; Yan, H.Q.; Wu, Y.Y.; Kind, H.; Weber, E.; Russo, R.; Yang, P.D. Room-Temperature Ultraviolet Nanowire Nanolasers. *Science* **2001**, *292*, 1897–1899. [CrossRef] [PubMed]
4. Tong, L.M.; Gattass, R.R.; Ashcom, J.B.; He, S.L.; Lou, J.Y.; Shen, M.Y.; Maxwell, I.; Mazur, E. Subwavelength-diameter silica wires for low-loss optical wave guiding. *Nature* **2003**, *426*, 816–819. [CrossRef]
5. Zhang, Q.; Liu, X.F.; Utama, M.I.B.; Xing, G.C.; Sum, T.C.; Xiong, Q.H. Phonon-Assisted Anti-Stokes Lasing in ZnTe Nanoribbons. *Adv. Mater.* **2016**, *28*, 276–283. [CrossRef]
6. Lu, Y.; Qu, K.; Zhang, T.; He, Q.; Pan, J. Metal Halide Perovskite Nanowires: Controllable Synthesis, Mechanism, and Application in Optoelectronic Devices. *Nanomaterials* **2023**, *13*, 419. [CrossRef]
7. Xing, G.C.; Mathews, N.; Lim, S.S.; Yantara, N.; Liu, X.F.; Sabba, D.; Grätzel, M.; Mhaisalkar, S.; Sum, T.C. Low-temperature solution-processed wavelength-tunable perovskites for lasing. *Nat. Mater.* **2014**, *13*, 476–480. [CrossRef]
8. Saidaminov, M.I.; Haque, M.A.; Almutlaq, J.; Sarmah, S.; Miao, X.H.; Begum, R.; Zhumekenov, A.A.; Dursun, I.; Cho, N.; Murali, B.; et al. Inorganic Lead Halide Perovskite Single Crystals: Phase-Selective Low-Temperature Growth, Carrier Transport Properties, and Self-Powered Photodetection. *Adv. Opt. Mater.* **2017**, *5*, 1600704. [CrossRef]
9. Pan, G.C.; Bai, X.; Xu, W.; Chen, X.; Zhai, Y.; Zhu, J.Y.; Shao, H.; Ding, N.; Xu, L.; Dong, B.; et al. Bright Blue Light Emission of Ni^{2+} Ion-Doped $CsPbCl_xBr_{3-x}$ Perovskite Quantum Dots Enabling Efficient Light-Emitting Devices. *ACS Appl. Mater. Interfaces* **2020**, *12*, 14195–14202. [CrossRef]
10. Eaton, S.W.; Lai, M.L.; Gibson, N.A.; Wong, A.B.; Dou, L.; Ma, J.; Wang, L.W.; Leone, S.R.; Yang, P.D. Lasing in robust cesium lead halide perovskite nanowires. *Proc. Natl. Acad. Sci. USA* **2016**, *113*, 1993–1998. [CrossRef]
11. Zhang, Q.; Su, R.; Liu, X.F.; Xing, J.; Sum, T.C.; Xiong, Q.H. High-Quality Whispering-Gallery-Mode Lasing from Cesium Lead Halide Perovskite Nanoplatelets. *Adv. Funct. Mater.* **2016**, *26*, 6238–6245. [CrossRef]
12. Wang, L.; Meng, L.H.; Chen, L.; Huang, S.; Wu, X.G.; Dai, G.; Deng, L.G.; Han, J.B.; Zou, B.S.; Zhang, C.F.; et al. Ultralow-Threshold and Color-Tunable Continuous-Wave Lasing at Room-Temperature from In Situ Fabricated Perovskite Quantum Dots. *J. Phys. Chem. Lett.* **2019**, *10*, 3248–3253. [CrossRef] [PubMed]
13. Bist, A.; Pant, B.; Ojha, G.P.; Acharya, J.; Park, M.; Saud, P.S. Novel Materials in Perovskite Solar Cells: Efficiency, Stability, and Future Perspectives. *Nanomaterials* **2023**, *13*, 1724. [CrossRef] [PubMed]
14. Song, J.Z.; Xu, L.M.; Li, J.H.; Xue, J.; Dong, Y.H.; Li, X.M.; Zeng, H.B. Monolayer and Few-Layer All-Inorganic Perovskites as a New Family of Two-Dimensional Semiconductors for Printable Optoelectronic Devices. *Adv. Mater.* **2016**, *28*, 4861–4869. [CrossRef] [PubMed]
15. Zhang, J.R.; Hodes, G.; Jin, Z.W.; Liu, S.Z. All-Inorganic $CsPbX_3$ Perovskite Solar Cells: Progress and Prospects. *Angew. Chem. Int. Ed.* **2019**, *58*, 15596–15618. [CrossRef]

16. Chen, J.Z.; Ma, G.B.; Gong, B.X.; Deng, C.Y.; Zhang, M.; Guo, K.X.; Cui, R.R.; Wu, Y.K.; Lv, M.L.; Wang, X. Bulk Photovoltaic Current Mechanisms in All-Inorganic Perovskite Multiferroic Materials. *Nanomaterials* **2023**, *13*, 429. [CrossRef] [PubMed]
17. Bao, C.X.; Yang, J.; Bai, S.; Xu, W.D.; Yan, Z.B.; Xu, Q.Y.; Liu, J.M.; Zhang, W.J.; Gao, F. High Performance and Stable All-Inorganic Metal Halide Perovskite-Based Photodetectors for Optical Communication Applications. *Adv. Mater.* **2018**, *30*, 1803422. [CrossRef]
18. Huang, S.Y.; Guo, M.L.; Tan, J.; Geng, Y.Y.; Wu, J.Y.; Tang, Y.W.; Su, C.C.; Lin, C.C.; Liang, Y. Novel Fluorescence Sensor Based on All-Inorganic Perovskite Quantum Dots Coated with Molecularly Imprinted Polymers for Highly Selective and Sensitive Detection of Omethoate. *ACS Appl. Mater. Interfaces* **2018**, *10*, 39056–39063. [CrossRef]
19. Wang, Y.; Lv, Z.Y.; Chen, J.R.; Wang, Z.P.; Zhou, Y.; Zhou, L.; Chen, X.L.; Han, S.T. Photonic Synapses Based on Inorganic Perovskite Quantum Dots for Neuromorphic Computing. *Adv. Mater.* **2018**, *30*, 1802883. [CrossRef]
20. Pourdavoud, N.; Haeger, T.; Mayer, A.; Cegielski, P.J.; Giesecke, A.L.; Heiderhoff, R.; Olthof, S.; Zaefferer, S.; Shutsko, I.; Henkel, A.; et al. Room-Temperature Stimulated Emission and Lasing in Recrystallized Cesium Lead Bromide Perovskite Thin Films. *Adv. Mater.* **2019**, *31*, 1903717. [CrossRef]
21. Yun, R.; Luo, L.; He, J.; Wang, J.; Li, X.; Zhao, W.; Nie, Z.; Lin, Z. Mixed-Solvent Polarity-Assisted Phase Transition of Cesium Lead Halide Perovskite Nanocrystals with Improved Stability at Room Temperature. *Nanomaterials* **2019**, *9*, 1537. [CrossRef] [PubMed]
22. Zhou, H.; Yuan, S.P.; Wang, X.X.; Xu, T.; Wang, X.; Li, H.L.; Zheng, W.H.; Fan, P.; Li, Y.Y.; Sun, L.T.; et al. Vapor Growth and Tunable Lasing of Band Gap Engineered Cesium Lead Halide Perovskite Micro/Nanorods with Triangular Cross Section. *ACS Nano* **2017**, *11*, 1189–1195. [CrossRef] [PubMed]
23. Yakunin, S.; Protesescu, L.; Krieg, F.; Bodnarchuk, M.I.; Nedelcu, G.; Humer, M.; De Luca, G.; Fiebig, M.; Heiss, W.; Kovalenko, M.V. Low-threshold amplified spontaneous emission and lasing from colloidal nanocrystals of caesium lead halide perovskites. *Nat. Commun.* **2015**, *6*, 8056. [CrossRef]
24. Fu, Y.P.; Zhu, H.M.; Stoumpos, C.C.; Ding, Q.; Wang, J.; Kanatzidis, M.G.; Zhu, X.Y.; Jin, S. Broad Wavelength Tunable Robust Lasing from Single-Crystal Nanowires of Cesium Lead Halide Perovskites ($CsPbX_3$, X = Cl, Br, I). *ACS Nano* **2016**, *10*, 7963–7972. [CrossRef] [PubMed]
25. Zhang, H.J.; Liu, X.; Dong, J.P.; Yu, H.; Zhou, C.; Zhang, B.B.; Xu, Y.D.; Jie, W.Q. Centimeter-Sized Inorganic Lead Halide Perovskite CsPbBr3 Crystals Grown by an Improved Solution Method. *Cryst. Growth Des.* **2017**, *17*, 6426–6431. [CrossRef]
26. Zeng, J.P.; Li, X.M.; Wu, Y.; Yang, D.D.; Sun, Z.G.; Song, Z.H.; Wang, H.; Zeng, H.B. Space-Confined Growth of $CsPbBr_3$ Film Achieving Photodetectors with High Performance in All Figures of Merit. *Adv. Funct. Mater.* **2018**, *28*, 1804394. [CrossRef]
27. Liu, P.; He, X.X.; Ren, J.H.; Liao, Q.; Yao, J.N.; Fu, H.B. Organic–Inorganic Hybrid Perovskite Nanowire Laser Arrays. *ACS Nano* **2017**, *11*, 5766–5773. [CrossRef]
28. Zhang, L.; Zhang, J.S.; Shang, Q.Y.; Song, J.P.; Li, C.; Du, W.N.; Chen, S.L.; Liu, X.F.; Zou, B.S.; Gao, P.; et al. Ultrafast Antisolvent Growth of Single-Crystalline $CsPbCl_3$ Microcavity for Low-Threshold Room Temperature Blue Lasing. *ACS Appl. Mater. Interfaces* **2022**, *14*, 21356–21362. [CrossRef]
29. Gebauer, D.; Kellermeier, M.; Gale, J.D.; Bergström, L.; Cölfen, H. Pre-nucleation clusters as solute precursors in crystallisation. *Chem. Soc. Rev.* **2014**, *43*, 2348–2371. [CrossRef]
30. Ravi, V.K.; Santra, P.K.; Joshi, N.; Chugh, J.; Singh, S.K.; Rensmo, H.; Ghosh, P.; Nag, A. Origin of the Substitution Mechanism for the Binding of Organic Ligands on the Surface of $CsPbBr_3$ Perovskite Nanocubes. *J. Phys. Chem. Lett.* **2017**, *8*, 4988–4994. [CrossRef]
31. Ghaithan, H.M.; Alahmed, Z.A.; Qaid, S.M.H.; Hezam, M.; Aldwayyan, A.S. Density Functional Study of Cubic, Tetragonal, and Orthorhombic $CsPbBr_3$ Perovskite. *ACS Omega* **2020**, *5*, 7468–7480. [CrossRef] [PubMed]
32. Abiedh, K.; Zaaboub, Z.; Hassen, F. Mixed monomolecular and bimolecular-like recombination processes in $CsPbBr_3$ perovskite film revealed by time-resolved photoluminescence spectroscopy. *Appl. Phys. A* **2021**, *127*, 623. [CrossRef]
33. Francisco-López, A.; Charles, B.; Weber, O.J.; Alonso, M.I.; Garriga, M.; Campoy Quiles, M.; Weller, M.T.; Goñi, A.R. Equal Footing of Thermal Expansion and Electron–Phonon Interaction in the Temperature Dependence of Lead Halide Perovskite Band Gaps. *J. Phys. Chem. Lett.* **2019**, *10*, 2971–2977. [CrossRef] [PubMed]
34. Niesner, D.; Schuster, O.; Wilhelm, M.; Levchuk, I.; Osvet, A.; Shrestha, S.; Batentschuk, M.; Brabec, C.; Fauster, T. Temperature-dependent optical spectra of single-crystal $(CH_3NH_3)PbBr_3$ cleaved in ultrahigh vacuum. *Phys. Rev. B* **2017**, *95*, 075207. [CrossRef]
35. Yu, C.; Chen, Z.; Wang, J.J.; Pfenninger, W.; Vockic, N.; Kenney, J.T.; Shum, K. Temperature dependence of the band gap of perovskite semiconductor compound $CsSnI_3$. *J. Appl. Phys.* **2011**, *110*, 063526. [CrossRef]
36. Wu, K.W.; Bera, A.; Ma, C.; Du, Y.M.; Yang, Y.; Li, L.; Wu, T. Temperature-dependent excitonic photoluminescence of hybrid organometal halide perovskite films. *Phys. Chem. Chem. Phys.* **2014**, *16*, 22476–22481. [CrossRef]
37. Shibata, K.; Yan, J.; Hazama, Y.; Chen, S.; Akiyama, H. Exciton Localization and Enhancement of the Exciton–LO Phonon Interaction in a CsPbBr3 Single Crystal. *J. Phys. Chem. C* **2020**, *124*, 18257–18263. [CrossRef]
38. Bimberg, D.; Sondergeld, M.; Grobe, E. Thermal Dissociation of Excitons Bounds to Neutral Acceptors in High-Purity GaAs. *Phys. Rev. B* **1971**, *4*, 3451–3455. [CrossRef]
39. Ai, B.; Liu, C.; Deng, Z.; Wang, J.; Han, J.J.; Zhao, X.J. Low temperature photoluminescence properties of $CsPbBr_3$ quantum dots embedded in glasses. *Phys. Chem. Chem. Phys.* **2017**, *19*, 17349–17355. [CrossRef]
40. Wright, A.D.; Verdi, C.; Milot, R.L.; Eperon, G.E.; Pérez-Osorio, M.A.; Snaith, H.J.; Giustino, F.; Johnston, M.B.; Herz, L.M. Electron–phonon coupling in hybrid lead halide perovskites. *Nat. Commun.* **2016**, *7*, 11755. [CrossRef]

41. Rudin, S.; Reinecke, T.L.; Segall, B. Temperature-dependent exciton linewidths in semiconductors. *Phys. Rev. B* **1990**, *42*, 11218–11231. [CrossRef] [PubMed]
42. Rudin, S.; Reinecke, T.L. Temperature-dependent exciton linewidths in semiconductor quantum wells. *Phys. Rev. B* **1990**, *41*, 3017–3027. [CrossRef] [PubMed]
43. Lan, S.G.; Peng, Y.Y.; Shen, H.Z.; Wang, S.; Ren, J.W.; Zheng, Z.P.; Liu, W.W.; Li, D.H. Seeds-Assisted Space-Confined Growth of All-Inorganic Perovskite Arrays for Ultralow-Threshold Single-Mode Lasing. *Laser Photonics Rev.* **2021**, *15*, 2000428. [CrossRef]
44. Guo, P.F.; Hossain, M.K.; Shen, X.; Sun, H.B.; Yang, W.C.; Liu, C.P.; Ho, C.Y.; Kwok, C.K.; Tsang, S.W.; Luo, Y.S.; et al. Room-Temperature Red–Green–Blue Whispering-Gallery Mode Lasing and White-Light Emission from Cesium Lead Halide Perovskite (CsPbX3, X = Cl, Br, I) Microstructures. *Adv. Opt. Mater.* **2018**, *6*, 1700993. [CrossRef]
45. He, X.X.; Liu, P.; Zhang, H.H.; Liao, Q.; Yao, J.N.; Fu, H.B. Patterning Multicolored Microdisk Laser Arrays of Cesium Lead Halide Perovskite. *Adv. Mater.* **2017**, *29*, 1604510. [CrossRef] [PubMed]
46. Schlaus, A.P.; Spencer, M.S.; Miyata, K.; Liu, F.; Wang, X.X.; Datta, I.; Lipson, M.; Pan, A.L.; Zhu, X.Y. How lasing happens in $CsPbBr_3$ perovskite nanowires. *Nat. Commun.* **2019**, *10*, 265. [CrossRef]
47. Hu, J.Y.; Wang, M.; Tang, F.W.; Liu, M.; Mu, Y.Y.; Fu, Y.L.; Guo, J.X.; Song, X.Y.; Zhang, X.P. Threshold Size Effects in the Patterned Crystallization of Hybrid Halide Perovskites for Random Lasing. *Adv. Photonics Res.* **2021**, *2*, 2000097. [CrossRef]
48. Liu, X.; Zhang, Q.; Xiong, Q.H.; Sum, T.C. Tailoring the Lasing Modes in Semiconductor Nanowire Cavities Using Intrinsic Self-Absorption. *Nano Lett.* **2013**, *13*, 1080–1085. [CrossRef]
49. Bade, S.G.R.; Li, J.; Shan, X.; Ling, Y.; Tian, Y.; Dilbeck, T.; Besara, T.; Geske, T.; Gao, H.; Ma, B.; et al. Fully Printed Halide Perovskite Light-Emitting Diodes with Silver Nanowire Electrodes. *ACS Nano* **2016**, *10*, 1795–1801. [CrossRef]
50. Tian, Y.X.; Peter, M.; Unger, E.; Abdellah, M.; Zheng, K.; Pullerits, T.; Yartsev, A.; Sundström, V.; Scheblykin, I.G. Mechanistic insights into perovskite photoluminescence enhancement: Light curing with oxygen can boost yield thousandfold. *Phys. Chem. Chem. Phys.* **2015**, *17*, 24978–24987. [CrossRef]